High Latitude Sea Surface Skin Temperatures Derived From Saildrone Infrared Measurements

Chong Jia , Peter J. Minnett , Malgorzata Szczodrak, and Miguel Izaguirre

Abstract—From May 15 to October 11, 2019, six Saildrone uncrewed surface vehicles (USVs) were deployed for 150-day cruises collecting a suite of atmospheric and oceanographic measurements from Dutch Harbor, Alaska, transiting the Bering Strait into the Chukchi Sea and the Arctic Ocean. Two Saildrones funded by the National Aeronautics and Space Administration (NASA), SD-1036 and SD-1037, were equipped with infrared (IR) radiation pyrometers in a "unicorn" structure on the deck for the determination of the ocean sea surface skin temperature (SST_{skin}). We present an algorithm to derive SST_{skin} from the downward- and upward-looking radiometers and estimate the main contributions to the inaccuracy of SST_{skin}. After stringent quality control of data and eliminating measurements influenced by sea ice and precipitation, and restricting the acceptable tilt angles of the USV based on radiative transfer simulations, SST_{skin} can be derived to an accuracy of approximately 0.12 K. The error budget of the derived SST_{skin} is developed, and the largest component comes from the instrumental uncertainties, assuming that the viewing geometry is adequately determined. Thus, Saildrones equipped with these sensors could provide sufficiently accurate SST_{skin} retrievals for studying the physics of the thermal skin effect, in conjunction with accurate subsurface thermometer measurements, and for validating satellite-derived SST_{skin} fields at high latitudes.

Index Terms—Arctic, infrared (IR) radiometer, Saildrone, sea surface skin temperature (SST_{skin}).

I. INTRODUCTION

SEA surface temperature (SST) is one of the most important variables in the global ocean-atmosphere system. It is a significant oceanic parameter and a key indicator of climate change, and is widely used to study the surface ocean dynamics [1], upper ocean interactions [2], heat exchange between ocean and atmosphere [3], marine biochemical process [4], and the carbon cycle [5]. Satellite remote sensing can, in principle, provide frequent, long-term, global coverage of the SST.

At present, satellite-derived SST is mainly calculated from the measurements of infrared (IR) and microwave radiometers, of which the IR sensors have a higher spatial resolution with a longer history of use, including the Advanced Very High Resolution Radiometer (AVHRR) [6], the Advanced Along-Track Scanning Radiometer (AATSR) [7], the Moderate Resolution Imaging Spectroradiometer (MODIS) [8], the Sea and Land Surface Temperature Radiometer (SLSTR) [9], [10], and the Visible Infrared Imaging Radiometer Suite (VIIRS) [11]. However, the measurements of the IR satellite sensors are susceptible to the effects of clouds, aerosols, and water vapor content in the atmosphere in their field of view. It is particularly difficult for IR satellite instruments to establish high-accuracy SST datasets at high latitudes [12], specifically in the Arctic region, compared with other areas of the global ocean due to the persistent cloud cover [13] and extremely dry and cold intervening atmosphere between the sea surface and the sensor apertures, which is a climatological extreme in the global distribution of atmospheric properties [14].

To better assess errors in the satellite SST retrievals, accurate in situ measurements are required as validation data. A comparative validation analysis is indispensable, being fundamental to the assessment of the satellite instrument performance and the accuracy of the retrieval algorithms, not only for SSTs but also for every geophysical variable retrieval from satellite measurements. The in situ measurements of SST taken by drifting buoys are the main source of validating data at high latitudes. Their sparsity results from the sea ice distribution and its seasonal variation [15], [16], especially at the northern Pacific side of the Arctic region (the Beaufort Sea, the Chukchi Sea, and the East Siberian Sea), given that there are large areas of year-round open water in Greenland, Norwegian, and Barents Seas in the Atlantic Ocean sector. Nevertheless, in recent years, due to the Arctic Amplification [17] effect of global warming, which has recently been assessed to be occurring at four times the global average [18], sea ice extent has significantly declined and retreated in the warmer months. Utilizing the sea ice melt-back, the meagerness in the Arctic SST in situ dataset has improved to some extent, which is beneficial to the research on verifying and developing the atmospheric correction algorithms used to retrieve SST [14], [19] and the quantification of satellite-derived SST accuracy [14], [20], [21]. It is worth mentioning that most in situ observations at high latitudes come from the drifting buoys, Upper Temperature of the polar Oceans (UpTempO) buoys [21], and some Argo floats [22], which measure the seawater temperature at depths of several

centimeters to meters underneath the sea surface, referred to as SST_{depth}. It is distinct from the sea surface skin temperature (SST_{skin}) representing the temperature within the conductive diffusion-dominated sublayer with a typical thickness of $\sim$10–20 μm, which gives rise to the IR emission measured by IR radiometers. Thus, the difference between SST_{skin} and SST_{depth} should be considered when validating the satellite data with subsurface temperature measurements. In nearly all conditions, SST_{skin} is cooler than SST_{depth}. The temperature drop, called the cool skin layer effect, is caused by surface cooling due to heat flow from the ocean to the atmosphere resulting from net long-wave radiation, latent heat flux, and sensible heat flux [23]. The thermal stratification in the uppermost ocean at low wind speeds with high insolation during the daytime, diurnal warming, causes a positive difference between SST_{skin} and SST_{depth} frequently >1 K and occasionally >5 K in highly stratified diurnal thermoclines [24], [25], [26]. However, even under conditions of diurnal heating, the thermal skin layer is nearly always negative as a result of heat loss to the atmosphere [27]. The contributions of the cool skin and diurnal heating to the validation using subsurface temperatures may erroneously be attributed to inaccuracies in the retrievals from measurements of satellite sensors, which clearly affects the estimation of the error made using in situ SST_{depth}. Considering that the use of SST_{depth} as the validation datasets introduce serious inadequacies for those regions characterized by large diurnal variability, IR radiometers mounted on ships or other platforms to measure the SST_{skin} have been recognized as providing appropriate, accurate surface measurements for the validation procedures.

Over the past several decades, efforts have been made to develop self-calibrating, shipborne thermal IR radiometer designs for measurements with a target accuracy of 0.1 K. There are several IR radiometer systems that have been proven to be successful in collecting SST_{skin} measurements from research vessels, such as the DAR011 radiometer [28], the Scanning Infrared Sea surface Temperature Radiometer (SISTeR) [29], the Ship of Opportunity Sea surface temperature Radiometer (SOOSR) [30], the Marine Atmospheric Emitted Radiance Interferometer (M-AERI) [31], the Calibrated Infrared In situ Measurement System (CIRIMS) [32], and the Infrared Sea surface temperature Autonomous Radiometer (ISAR) [33]. Despite notable progress, the frequent collection of worldwide ship-based SST_{skin} data is still an aspiration of the communities aiming to validate satellite-derived SSTs. The amount of available SST_{skin} validation data is limited in number and spatiotemporal extent, especially at high latitudes. The main challenge for acquiring more data is that the deployment and maintenance of accurate radiometers are both difficult and expensive. Although the radiometers mentioned above are capable of providing high-quality SST_{skin} data, some have no means to protect themselves against hostile marine environments during autonomous deployment. Even the M-AERI, SISTeR, and ISAR, which possess automatic safe-mode mechanisms, are difficult to deploy on small platforms due to their large physical size, weight, and power requirements.

This article introduces measurements from a simple system with two IR radiation pyrometers carried on Saildrones, uncrewed surface vehicles (USVs). Saildrone Inc. designs and manufactures a fleet of trusted and capable USVs for marine scientific research missions. Saildrones are predominantly powered by wind and solar, and are equipped with advanced meteorological and oceanographic instruments and artificial intelligence technology to deliver valuable data wherever their mission takes them. Prior to the Arctic Saildrone Cruise in 2019 of the third Multi-Sensor Improved Sea Surface Temperature Project (MISST-3) [34], [35], some Saildrones usually carried a single down-looking IR pyrometer mounted on the wing spar protruding from the wing. The 2019 Arctic deployment included two additional IR pyrometers installed on the decks of two Saildrones: one to measure the sea surface emission plus a reflected component of the sky emission and the other pointing upward at the same zenith angle as the sea-viewing sensor is to the nadir to obtain the contemporaneous downwelling atmospheric emission for the correction of reflected sky radiance.

We introduce the IR radiometric sensors on two Saildrones during the 2019 Arctic Cruise. First, a brief description of Saildrone is given in Section II. The design and operating principle of the IR pyrometers to measure IR radiance are elaborated in Section III. We use the data from the Arctic mission to make comparisons between the SST_{skin} retrievals from the wing and the hull pyrometers of the Saildrones and between two drones within small spatial separations in Section IV. We also assess and analyze the error budget for the derived SST_{skin} in Section IV. Finally, the summary is made in Section V.

II. SAILDRONE

USVs, also known as autonomous surface vehicles (ASVs), are boats or ships operating on the water surface without a crew. Initially, USVs were applied to the clearance of mines after World War II. With years of development, the applications of USVs are more than for the military but are also valuable in oceanography [36], [37], [38]. The USVs are much cheaper than conventional research vessels and more adaptable to changing conditions than voluntary observing ships. It is foreseeable that USVs could substantially contribute to the global ocean observing system with more numerous deployments in the future. Here, in Sections II-A and II-B, we will introduce a representative USV platform Saildrone and the Arctic cruise in 2019.

A. Overview

Saildrone, as one of the most capable USV platforms, provides atmospheric and oceanic measurements using autonomous technology for long-term missions of up to 12 months. These vehicles operate exclusively on sustainable energy, combining wind power for propulsion and a suite of solar-powered meteorological and oceanographic sensors (see Fig. 1). Each vehicle is comprised of a 7-m narrow hull, a 5-m high hard wing, and a keel with a 2.5-m draft, with a weight

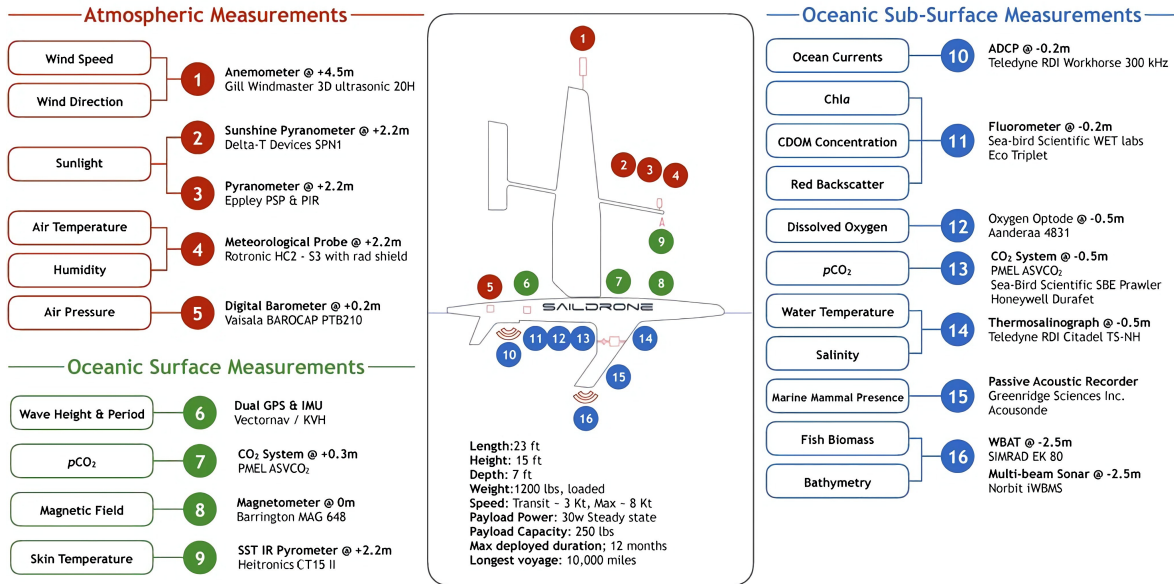## SAILDRONE GEN 4 SPECIFICATIONS AND SENSOR SUITE

Fig. 1. Saildrone (generation 4) standard configuration and generally installed scientific instruments. Additional subsurface thermometers were installed on the keel for the MISST-3 2019 deployment. Note that "9" is named skin temperature but it is a measurement of upwelling IR radiation without the correction for sky radiance reflected at the sea surface. Courtesy Saildrone. Used with express permission.

of approximately 750 kg and which sails at an average speed of ∼1.5 m/s (maximum up to 4 m/s).

Each Saildrone has been equipped with ∼15 science-grade sensors (the number can be adjustable on demand) collecting important atmospheric and oceanographic data generally including barometric pressure, air temperature and relative humidity, wind speed and direction, solar irradiance, surface IR emission, subsurface ocean temperature, salinity, chlorophyll fluorescence, dissolved oxygen, and wave height and period. The sensors are connected to onboard computers and deliver data in real time via satellite transmissions to ground stations, making adaptive sampling and real-time data analysis possible. The position and operating conditions of the Saildrone USVs are also transmitted via satellite and monitored by human pilots, controlling the autonomous navigation from prescribed waypoint to waypoint, accounting for wind and currents, while staying within a user-defined corridor. To further guarantee the safety of the cruise, each vehicle is equipped with an automated identification system (AIS) transceiver, navigation lights, radar reflector, high visibility wing colors, and four cameras aboard imaging up, down, port, and starboard of the wing [39].

B. Cruise Description

From May 15 to October 11, 2019, a fleet of Saildrone vehicles made a 150-day round-trip cruise from Dutch Harbor, Alaska. This deployment involved six Saildrones (SD-1033, SD-1034, SD-1035, SD-1036, SD-1037, and SD-1041) and was a research collaboration between the National Aeronautics and Space Administration (NASA), the National Oceanic and Atmospheric Administration's (NOAA's) Pacific Marine Environmental Laboratory (PMEL) and Alaska Fisheries Science

Center (AFSC), and the NOAA/University of Washington Joint Institute for the Study of the Ocean and Atmosphere (JISAO). This article focuses on the NASA-funded vehicles, SD-1036 and SD-1037, which are the two Saildrones carrying a pair of IR pyrometers on the deck for the SST_{skin} retrieval. SD-1036 and SD-1037 navigated north through the Bering Strait into the Chukchi Sea, then back and forth transects in the Chukchi Sea, and approached the southern sea ice edge of the Arctic Ocean up to ∼75° N by the beginning of August (see Fig. 2). Due to the solar power constraints caused by low sun elevation angles, some sensors were required to be turned off or to reduce the sampling intervals during the return trip. Data from the Arctic field campaign in 2019 are openly available at the NASA Physical Oceanography Distributed Active Archive Center (PO.DAAC). Further information and resources can be found online (https://podaac.jpl.nasa.gov/Saildrone).

III. MEASURING RADIOMETRIC SKIN TEMPERATURE FROM SAILDRONES

A. Basic Principle of Shipborne Radiometer Measurement for SSTskin

The fundamental principle of determining the SST_{skin} using IR radiometers is measuring the IR radiation emitted by the sea surface over a limited spectral bandwidth and inverting the Planck function. Nevertheless, the emissivity (ε) of seawater is slightly less than unity at the IR wavelengths, λ, of interest resulting in a small portion of downwelling atmospheric radiation being reflected at the air–sea interface into the field of view (FOV) of the sea-viewing radiometer. The derived SST_{skin} would be inaccurate if the reflected sky radiance were not taken into account. As a result, to measure SST_{skin} within sufficient accuracy for scientific applications, simultaneous,
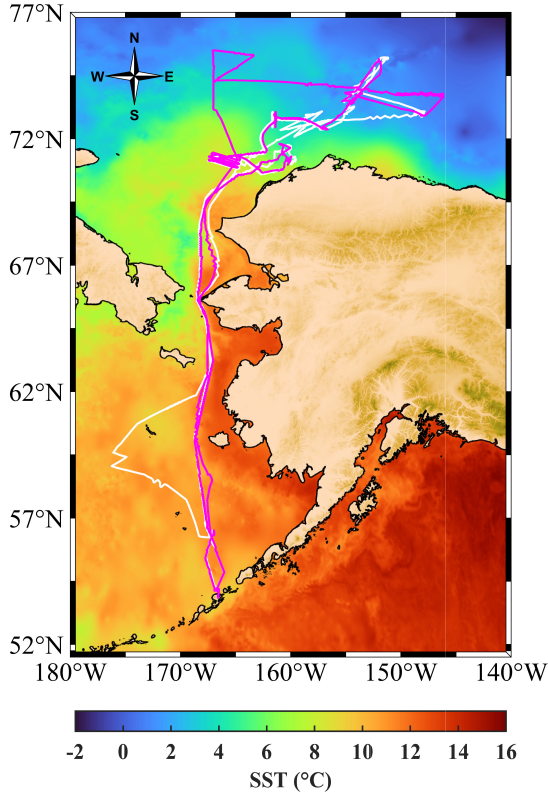
Fig. 2. Cruise tracks for the 2019 Arctic Saildrone deployments SD-1036 (white) and SD-1037 (magenta). The background SSTs on September 16, 2019, are from Multiscale Ultrahigh Resolution (MUR) Level 4 SST analysis data [40] produced by the Group for High Resolution Sea Surface Temperature (GHRSST; https://www.ghrsst.org/) and available from the NASA PO.DAAC.
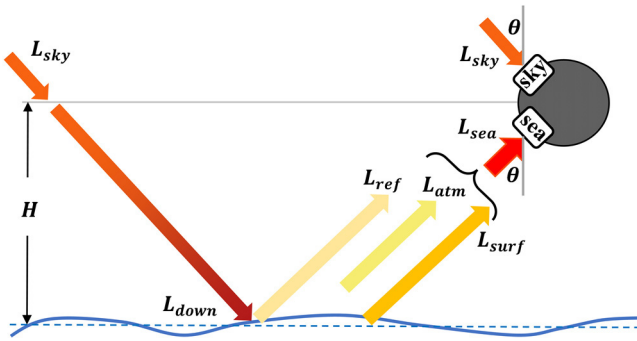

Fig. 3. Geometrical sketch of radiative components taken into account for measuring SST_{skin} with a dual-port IR radiometer mounted on a ship or a platform at a height of H viewing the sea surface and sky at θ.

or near-simultaneous, measurements of both the upward radiance from the direction of the sea surface and the downward radiance emitted from the atmosphere must be acquired at the appropriate viewing angles. Fig. 3 shows the geometrical arrangement of spectral radiance components which must be considered when deriving the SST_{skin} radiometrically.

Consider an IR radiometer installed on a platform at a height of H above the waterline, viewing the ocean surface at temperature T_s at a nadir angle θ. The sea surface is assumed to be flat, that is to say, the reflected sky radiation into the FOV of the sensor originates from a zenith angle θ. Also, assuming a homogeneous atmospheric path within the layer beneath the instrument of depth H, then the downward atmospheric radiance, $L_{\text{down}}(\lambda, \theta)$, at the sea surface can be given by

$$L_{\text{down}}(\lambda, \theta) \approx \tau_H L_{\text{sky}}(\lambda, \theta) + (1 - \tau_H)\overline{B(T_a, \lambda)} \quad (1)$$

where $L_{\text{sky}}(\lambda, \theta)$ is the incident atmospheric radiance at height H, which is the measurement of the sky-viewing radiometer. τ_H is the transmittance along $H \sec \theta$, the path from the instrument to the sea surface, and $B(T, \lambda)$ is the Planck function giving the emitted energy from a blackbody. $\overline{B(T_a, \lambda)}$ is the average radiated emission at atmospheric temperature T_a along the path $H \sec \theta$. The upward radiance from the sea surface is composed of the reflected $L_{\text{down}}(\lambda, \theta)$ and sea surface emission, and is expressed by

$$L_{\text{up}}(\lambda, \theta) = L_{\text{surf}}(\lambda, \theta) + L_{\text{ref}}(\lambda, \theta)$$
$$= \varepsilon(\lambda, \theta)B(T_s, \lambda) + (1 - \varepsilon(\lambda, \theta))L_{\text{down}}(\lambda, \theta). \quad (2)$$

Considering the atmospheric emitted radiance along the path, $L_{\text{atm}}(\lambda, \theta)$, the spectral radiation finally reaching the sea-viewing radiometer is given by

$$L_{\text{sea}}(\lambda, \theta) \approx \tau_H L_{\text{up}}(\lambda, \theta) + (1 - \tau_H)\overline{B(T_a, \lambda)}. \quad (3)$$

Substituting (1) and (2) into (3)

$$L_{\text{sea}}(\lambda, \theta) = \tau_H \varepsilon(\lambda, \theta)B(T_s, \lambda) + \tau_H^2(1 - \varepsilon(\lambda, \theta))L_{\text{sky}}(\lambda, \theta)$$
$$+ (1 - \tau_H)[(1 - \varepsilon(\lambda, \theta))\tau_H + 1]\overline{B(T_a, \lambda)}. \quad (4)$$

B. Radiometric Measurement System on Saildrones

Saildrones SD-1036 and SD-1037 deployed in the 2019 Arctic Mission, carried three IR radiation pyrometers; one was mounted on the spar of the sail at 2.25 m above the ocean surface, and the other two were situated near the bow on the deck at a height of 0.8 m viewing the sea surface and the sky at the same nadir angle and zenith angle, as shown in Fig. 4(a). Heights are given for an upright Saildrone. The pyrometers were manufactured by Heitronics Infrarot Messtechnik GmbH; the two sea-viewing sensors were CT15.10s [hereafter CT15; Fig. 4(c)], while the sky-viewing sensor was a CT09.10 [hereafter CT09; Fig. 4(b)]. The measurement specifications for both CT09 and CT15 are listed in Table I. Both have the merits of fast response times, long-term stability, and temperature stability due to the Heitronics chopped radiation measurement method. Yet, the performance of CT09 is obviously inferior to that of CT15, and it has been deemed to be acceptable because of the reduced accuracy requirement for the downwelling sky radiance measurements (as shown in Section III-C). Despite that the spectral responses of both CT09 and CT15 are mostly in the $8 - 14$-μm wavelength range, as shown in Fig. 5, their differences might cause inaccuracies in the derived SST_{skin}, which are also evaluated in Section III-C. In view of the low installation heights for the instruments, the atmospheric transmittance τ_H is very close to unity in the IR spectral region of concern. Equation (4) is then simplified to become

$$L_{\text{sea}}(\lambda, \theta) = \varepsilon(\lambda, \theta)B(T_s, \lambda) + (1 - \varepsilon(\lambda, \theta))L_{\text{sky}}(\lambda, \theta). \quad (5)$$

TABLE I

SOME MANUFACTURER'S SPECIFICATIONS FOR HEITRONICS IR PYROMETERS CT09 AND CT15

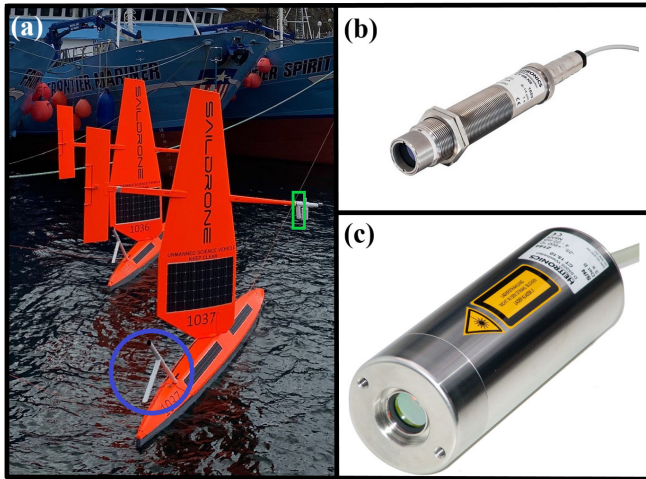|	CT09	CT15
Temperature range	-30 to 500 ℃ (option as low as -100 ℃)	-25 to 900 ℃
Spectral response	8 to 14 μm	8 to 14 μm
Measurement uncertainty	± 1.0 ℃ plus 0.6% of the difference between target and instrument temperature	± 0.5 ℃ plus 0.7% of the difference between target and instrument temperature
Temperature resolution (NEΔT)	Typical value 0.1 ℃	Typical value 0.03 ℃
Long-term stability	Better than 0.01% of the absolute measured value per month	Better than 0.01% of the absolute measured value per month
Field of view	From Ø 1.0 mm, depending on optics	From Ø 0.7 mm, depending on optics. For Saildrone CT15s, the FOV on the sea surface is ~ 5×10^{-3} m^{-2}
Response time	50 ms to 10 s	30 ms to 600 s

Fig. 4. (a) SD-1036 and SD-1037 deployed during the 2019 Arctic Cruise prior to departure from Dutch Harbor, Alaska. Two Heitronics IR radiometers with a "unicorn" structure were mounted on the hull as circled in blue, one mounted on the tip of the spar in the green box. Courtesy Saildrone. Used with express permission. (b) Heitronics CT09 Series IR radiation pyrometer and (c) CT15.10 IR radiation pyrometer. From https://www.heitronics.com/.
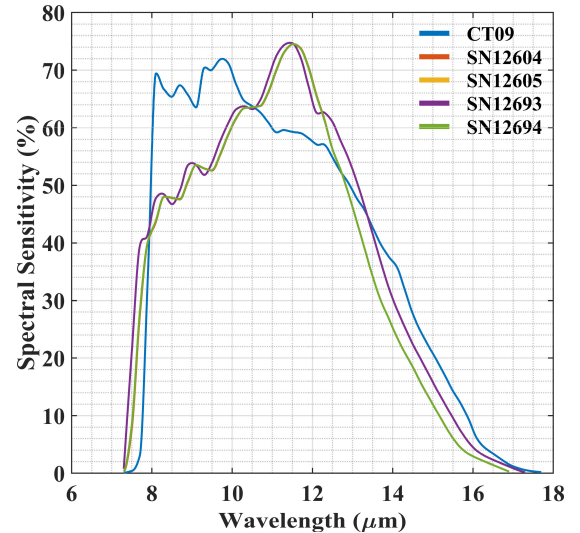

Fig. 5. Normalized spectral sensitivity of Heitronics CT09 and four specific CT15 IR radiation thermometers. Note that the SN12693 profile slightly diverges from the other three CT15s presumably due to the use of a different batch of optical elements. Due to the very high similarity, the spectral response function curves for SN12604 and SN12605 are underneath that of SN12693.

Unlike the CT09s that do not have individual specification data for each unit, the CT15s have their own performance data. The four CT15s with serial numbers (SNs) 12 604, 12 605, 12 693, and 12 694 installed on SD-1036 and SD-1037 show almost perfectly consistent spectral response profiles except for SN12693, which has slight differences (see Fig. 5). To compensate for these discrepancies, the normalized relative spectral response (RSR) functions corresponding to the IR radiometer in service must be incorporated into the calculations for the radiance. The output signal from sea-viewing radiometers on the Saildrones, R_{sea}, is then given by

$$R_{\text{sea}} = \int_{\lambda_0}^{\lambda_1} \sigma(\lambda)[\varepsilon(\lambda,\theta)B(T_s,\lambda)(1-\varepsilon(\lambda,\theta))L_{\text{sky}}(\lambda,\theta)]d\lambda \quad (6)$$

where the RSR function $\sigma(\lambda)$ of the CT15 instrument defines the limits of integration in (6). For Saildrones, CT09 is incapable of measuring $L_{\text{sky}}(\lambda,\theta)$, and instead an equivalent atmospheric temperature, or called sky temperature, T_{sky}, is taken. T_{sky} is an average over the RSR function of CT09, in which variations occur because of the wavelength dependence of atmospheric transmission. Equation (6) then becomes

$$R_{\text{sea}} = \int_{\lambda_0}^{\lambda_1} \sigma(\lambda)[\varepsilon(\lambda,\theta)B(T_s,\lambda)$$
$$+ (1-\varepsilon(\lambda,\theta))B(T_{\text{sky}},\lambda)]d\lambda. \quad (7)$$

According to (7), it is necessary to know accurately the viewing geometry and the sea surface emissivity for the spectral intervals. The equation presumes a flat ocean surface
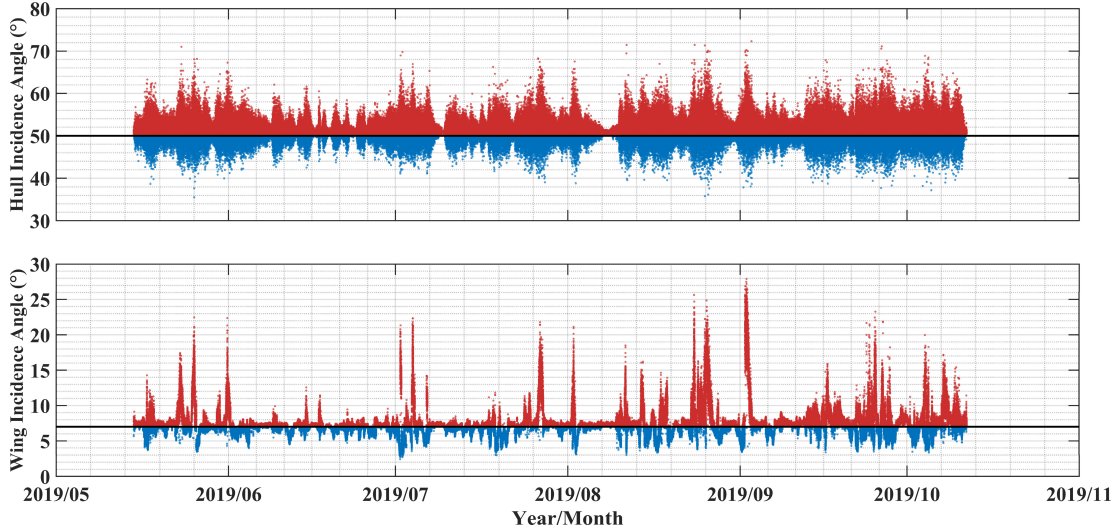
Fig. 6. Time series of the absolute viewing angle θ_e of the downward-looking IR pyrometers installed on (top) SD-1036 hull and (bottom) wing. The horizontal black lines separate the incidence angle at 50° and 7°, distinguishing in red (above) and blue (below).

without any tilted facets, as mentioned above, which means that the reflected downwelling atmospheric radiance originates from the look angle of the sea-viewing IR pyrometer, θ. However, it does not follow that θ is constant considering the effect of wind and wave motions tilting the Saildrones. The effective incidence angle of radiance into the sensor must be well determined since it has a role in the sea surface emissivity calculation; in particular, the sensitivity of emissivity values is high at large θ. Establish the 3-D rotation matrix

$$R = \begin{bmatrix} \cos\gamma & -\sin\gamma & 0 \\ \sin\gamma & \cos\gamma & 0 \\ 0 & 0 & 1 \end{bmatrix} \begin{bmatrix} \cos\beta & 0 & \sin\beta \\ 0 & 1 & 0 \\ -\sin\beta & 0 & \cos\beta \end{bmatrix} \cdots$$
$$\cdots \begin{bmatrix} 1 & 0 & 0 \\ 0 & \cos\alpha & -\sin\alpha \\ 0 & \sin\alpha & \cos\alpha \end{bmatrix} R' \quad (8)$$

where R and R' are the coordinate vectors in the geodetic reference frame and the local reference frame, respectively. γ is the angle rotating about the z-axis, the yaw angle; β is the angle rotating about the y-axis, the pitch angle; and α is the angle rotating about the x-axis, the roll angle. Those angles for both the wing and hull of Saildrone were measured by the inertial measurement unit (IMU) carried on the vehicles. The unit vector with reference to the IR pyrometer itself can be expressed by

$$R' = \begin{bmatrix} \cos\theta_0 & 0 & \sin\theta_0 \\ 0 & 1 & 0 \\ -\sin\theta_0 & 0 & \cos\theta_0 \end{bmatrix} \begin{bmatrix} 0 \\ 0 \\ 1 \end{bmatrix} \quad (9)$$

where θ_0 is the standard viewing angle of the instruments for an upright Saildrone. Then, the effective incidence angle θ_e is given by

$$\theta_e = \arccos\left(R \cdot \begin{bmatrix} 0 \\ 0 \\ 1 \end{bmatrix} \right). \quad (10)$$

For the sensors mounted on the hull, θ_0 is $-50°$ (down-looking) or 50° (up-looking); for the sensors at the spar of the
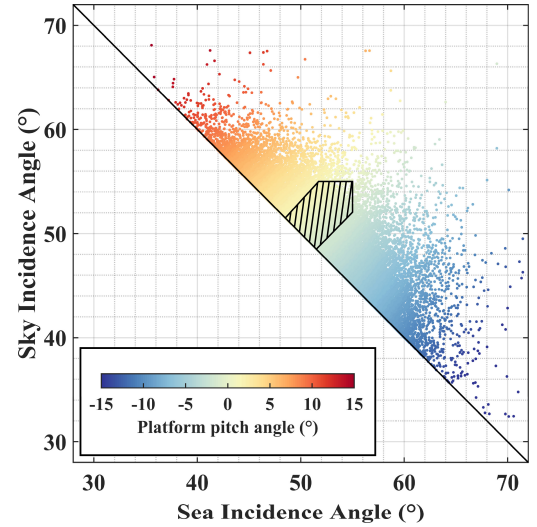

Fig. 7. Absolute effective incidence angle of radiance, θ_e, for the sky-viewing and sea-viewing radiometers mounted on the hull of SD-1036 are colored by the pitch angles. The area with diagonals indicates the ranges of θ_e reserved for sky corrections and further analysis.

wing, θ_0 is $-7°$ relative to an upright Saildrone. Fig. 6 shows the time series of the calculated θ_e. For both hull and wing, θ_e deviates significantly from the nominal angle due to the Saildrone tilt. It should be noted that both the rolling and pitching of the vehicle impact θ_e of the sensors and the larger pitch angles result in greater θ_e differences between up-looking and down-looking hull pyrometers (see Fig. 7). This indicates the term $B(T_{\text{sky}}, \lambda)$ in (7), measured by the sky-viewing instrument, would introduce some errors in the SST_{skin} derivation due to the atmospheric radiation transfer along different paths to the surface (see Section III-C).

With the determination of viewing geometry, the sea surface emissivity, $\varepsilon(\lambda, \theta_e)$, for the IR spectrum and incidence angle of radiance should be determined more accurately. We calculated $\varepsilon(\lambda, \theta_e)$ using a fast radiative transfer model, radiative transfer
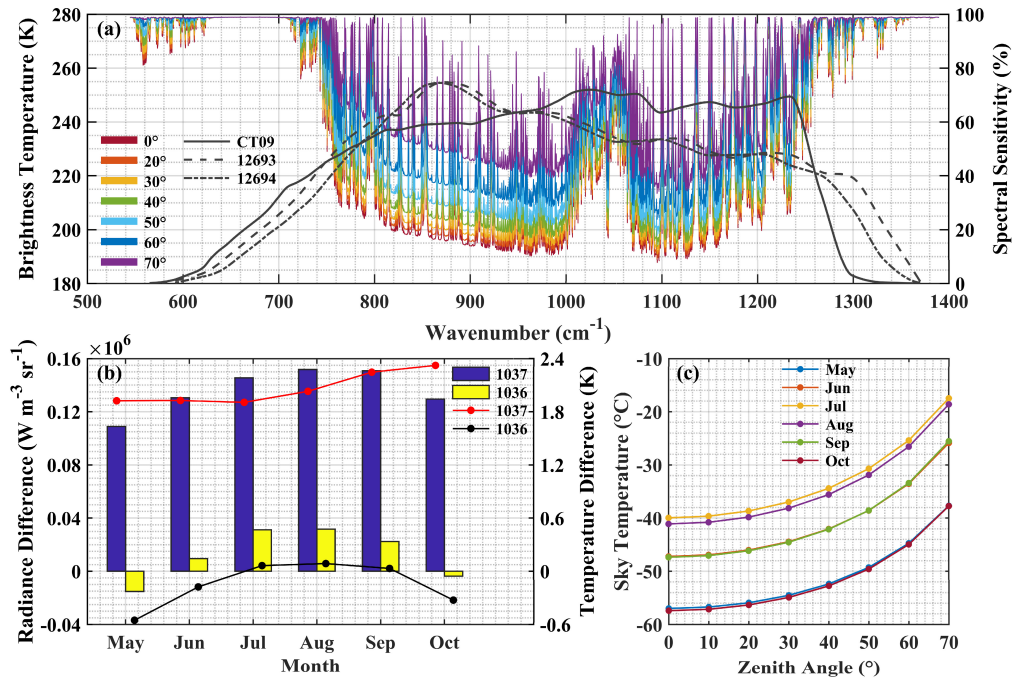
Fig. 8. LBLRTM simulations for (a) clear sky spectrum of downwelling IR radiance (in terms of brightness temperature) at the surface for the mean atmospheric condition of June in the study region at a range of zenith angles, plotted with curves of the RSR functions for CT09 (solid), SN12693 on SD-1037 (dashed), and SN12694 on SD-1036 (dashed-dotted), (b) monthly incident radiance (bars) and corresponding measured sky temperature difference (dots and lines) between SN12693 or SN12694 minus CT09 due to their different RSR functions at a zenith angle of 50°, and (c) zenith angle effects on CT09 measured sky temperatures in each month.

for TIROS operational vertical sounder (RTTOV) [41], which has a built-in IR sea surface emissivity (IREMIS) model. This model was developed for the IR emissivity simulation since RTTOV version 12, which includes the zenith angle and wind speed dependence, also the refractive indices depending on skin temperature in the 10–12-μm window [42]. More detailed descriptions of the emissivity formulation are in Saunders et al. [43]. To characterize the $\varepsilon(\lambda, \theta_e)$ variation over the IR wavelength range of CT15s, the RTTOV coefficient file for a hyperspectral sounder, the FORUM Sounding Instrument (FSI), is used for the simulations. The Far-infrared Outgoing Radiation Understanding and Monitoring (FORUM) mission has been selected to be the ninth Earth Explorer mission of the European Space Agency (ESA) [44], which aims to fill the measurement gap of top of atmosphere (TOA) emission in the far IR (wavelengths from 15 to 100 μm) for the better scientific understanding of the far IR contributions to the Earth's outgoing long-wave radiation. FSI is a sophisticated Fourier Transform Spectrometer with 5001 spectral samples, aligned between 100 and 1600 cm^{-1} (100 and 6.25 μm) with a sampling interval of 0.3 cm^{-1}. Using the viewing geometries obtained from (10), wind speeds measured by the anemometer located above the sail of Saildrone at 5 m, and the IR temperature measurements from CT15 on the Saildrones as the first approximations of skin temperature, RTTOV outputs the sea surface emissivity values for the spectral interval of FSI for the range of conditions considered in this article.

C. Evaluation of Sky Radiation Measurements on Saildrones

Before deriving SST$_{skin}$, we have to control the quality of the up-looking radiometer measurements since both the

different RSR functions and the different θ_e angles between CT09 and CT15 mounted on the deck introduce inaccuracies in correcting the reflected sky radiance. The consequences are shown in this section. To begin with, we use the accurate Line-By-Line Radiative Transfer Model (LBLRTM) [45] to simulate clear sky atmospheric downwelling radiance spectra at the surface, and then, the simulated radiances (and corresponding brightness temperatures) measured by the IR pyrometers are calculated with the RSR functions in Fig. 5. The data from Modern-Era Retrospective analysis for Research and Applications, Version 2 (MERRA-2) [46], a global atmospheric reanalysis produced by the NASA Global Modeling and Assimilation Office (GMAO), are chosen as the model inputs, including profiles of atmospheric temperature, specific humidity (water vapor), ozone, and surface meteorological fields. The carbon dioxide, methane, and nitrous oxide profiles are also included in the simulations as fixed gases, using the mean of a set of 80 atmospheric profiles containing diverse atmospheric conditions selected from the database generated by the experimental suite (cycle 30R2) of the European Centre for Medium-Range Weather Forecasts (ECMWF) forecasting system [47]. The input MERRA-2 assimilation meteorological data have been taken as the monthly average in the target area (50° N–75° N, 180° W–140° W) excluding data over land. Fig. 8(b) shows the simulations of the radiance (and corresponding temperature) differences measured by SN12693 or SN12694 and CT09 at a zenith angle of 50° from May to October 2019. Both of them vary slightly by month because of the seasonal changes in the atmosphere. The discrepancies in sky radiance in each month (as well as corresponding T_{sky}) are much more conspicuous for SN12693 on SD-1037
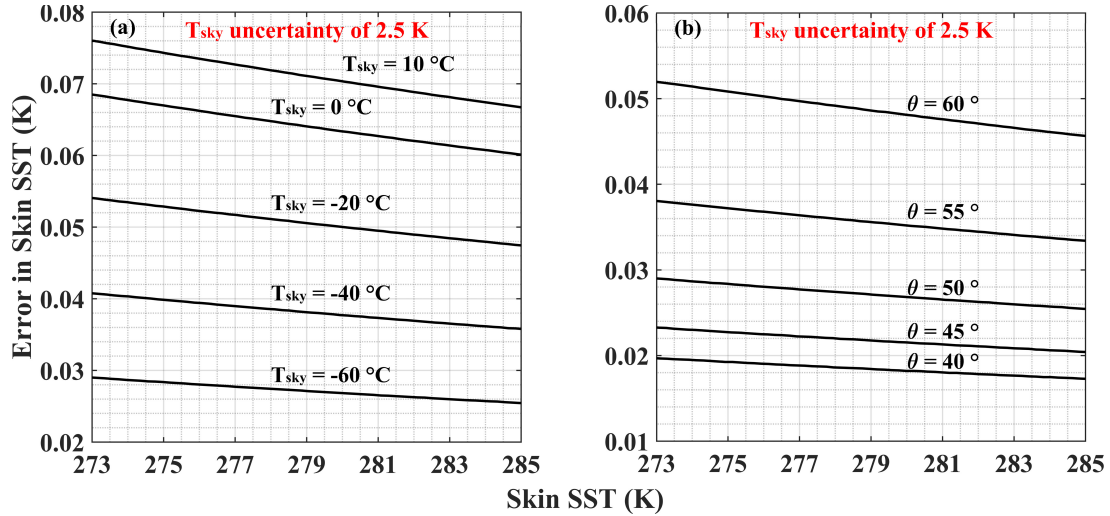
Fig. 9. Numerical tests for the SST_{skin} error introduced by sky radiometric temperatures with an uncertainty of 2.5 K (a) at a fixed zenith angle of 50° at various sky temperatures and (b) under a clear sky (−60 °C) but at different viewing angles.

than SN12694 on SD-1036 due to the broader bandwidth of SN12693 (see Fig. 5).

To further examine the effects of inconsistent θ_e between the up- and down-looking radiometers due to the pitching of the vehicle, the zenith angle was set from 0° to 70° in increments of 10° based on the simulation described above. Fig. 8(a) illustrates the spectra, represented as brightness temperature, simulated by LBLRTM for the mean atmospheric profile of June at varying zenith angles, where lower sky temperatures indicate the more transmissive atmosphere. As shown in Fig. 8(c), the zenith angle affects the T_{sky} dramatically over 50°, which persuades us to restrict the limits of θ_e for analysis to reduce the inaccuracy in using T_{sky}. The T_{sky} difference could reach ∼13 K at a sea-viewing θ_e of 65° and a sky-viewing θ_e of 35°, or conversely. Therefore, the uncertainties in the derived SST_{skin} introduced by those in T_{sky} are estimated to determine the accuracy tolerance in the sky measurements. As shown in Fig. 9(a), for a 2.5 K uncertainty of T_{sky} and at a zenith angle of 50°, the maximum SST_{skin} error is approximately 0.03 K under clear skies (−60 °C). Fig. 9(b) demonstrates the sea surface emissivity effect on the SST_{skin} correction under clear skies, and it is especially pronounced over 50° since ε decreases more rapidly with larger zenith angles. Thus, the ranges of the sea- and sky-viewing θ_e angles to be used in SST_{skin} derivations are both limited to 45° to 55° first. However, it is not sufficient as there still could be ±10° discrepancies in θ_e that brings about up to ±4.5 K biases in T_{sky}. Thus, the platform pitch angle is also limited within ±1.5° to further minimize the inaccuracy in the use of sky measurements and the emissivity effect at the cost of reducing the available data by ∼30%, which is acceptable. Due to those constraints, the sea and sky θ_e differences have been finally controlled within ±3° (see Fig. 7), and the resulting T_{sky} uncertainties are <±1.5 K, which introduces a maximum error in the derived SST_{skin} < 0.02 K under clear sky conditions. The error under overcast skies is not determined quantitatively here since the first priority of Saildrone SST_{skin} data is to validate satellite IR SST_{skin} retrievals, which are

only feasible through clear skies. Nonetheless, what is certain is that the downward sky radiation at the surface for cloudy skies would not change with the zenith angle as significantly as for clear skies due to the shorter atmospheric path length and a smaller difference between T_{sky} and SST_{skin}. Thus, we infer that the SST_{skin} errors due to sea- and sky-viewing θ_e difference under cloudy skies should be comparable or smaller to those under clear skies. Recall that the use of T_{sky} has another source of error due to the dissimilar spectral response functions between CT09 and CT15, as simulated above. For SD-1036, CT09 generally measures T_{sky} 0.15 K warmer than that would have been measured by SN12694 under clear skies, whereas, for SD-1037, it reaches up to 2 K colder on average. Consequently, the resulting SST_{skin} error could be ignored for SD-1036 but is more significant for SD-1037 as it could introduce a warm bias of 0.025 K under clear skies.

IV. RESULTS AND DISCUSSION

A. Derivation of SST_{skin} From Hull and Wing Measurements

Given the IR sea and sky radiometric measurements from Saildrones, well-approximated ε values, and the known RSR functions of CT15s, SST_{skin} can be derived based on (7). Note that the sea-viewing radiometric sensor installed on the wing has no matched sky-viewing sensor, and thus, the wing measurements have to be corrected by other means, for example using T_{sky} measured by the sky-viewing radiometer on the hull. This might lead to inappropriate corrections for the SST_{skin} derived from the wing (denoted as SST_{wing}) because of the large θ_e discrepancies between the hull and wing IR pyrometers (see Fig. 6); however, from Fig. 10, the ε values for SST_{wing} determination are less variable and closer to unity than those for the SST_{skin} derived from hull (denoted as SST_{hull}), which means that the reflectivity term, $1 − \varepsilon(\lambda, \theta)$, in (7) is smaller, and inaccurate T_{sky} should be less effective in causing the error of SST_{wing}. Therefore, it is meaningful to make comparisons between contemporaneous SST_{hull} and SST_{wing} derivations. Fig. 11(a) shows the time series for the SD-1036
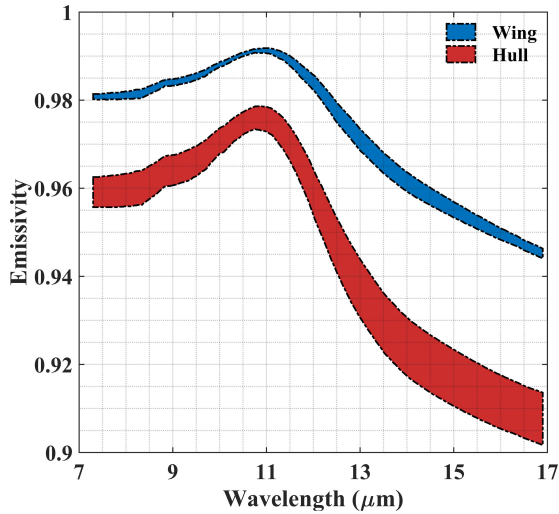
Fig. 10. Ranges of the sea surface emissivity in the spectral interval of concern determined for the derivation of Saildrone SST_{hull} (red) and SST_{wing} (blue).
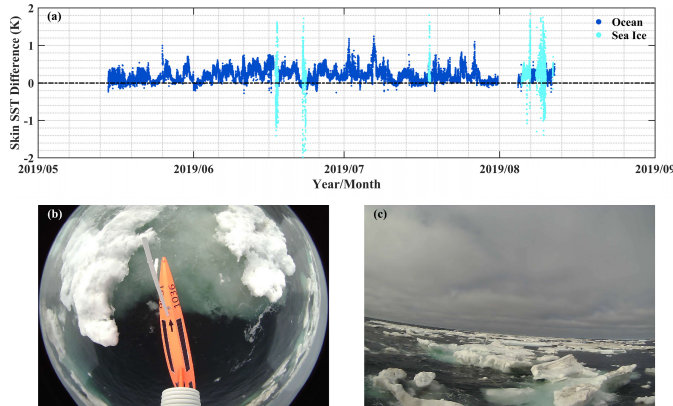

Fig. 11. (a) Time series of the temperature difference between SST_{hull} and SST_{wing} from SD-1036. The data points are colored in either dark blue or light blue, indicating when the vehicle navigated in the open ocean or close to the edge of sea ice. (b) and (c) Images taken by the cameras onboard SD-1036 at 1:02 UTC on July 18, 2019, in two different FOVs. Images courtesy Saildrone. Used with express permission.

temperature difference of SST_{hull} minus SST_{wing}. The data only lasted till the beginning of August as the IR pyrometers were subsequently turned off due to the lack of sufficient sunlight to maintain adequate power levels. Both large positive and negative differences are distinct at certain periods, which are identified in images recorded by the cameras onboard as sea ice contamination [see Fig. 11(b) and (c)]. SD-1036 and SD-1037 first encountered the edge of free-floating sea ice on June 17, 2019, and there were several subsequent encounters during the cruises. Depending on the distribution of ice around the Saildrone, either SST_{hull} or SST_{wing} could represent the temperature of ice or water chilled by ice melt when the Saildrone was close to, or in, sea ice. Removing those dubious measurements, the SST_{hull} values are generally warmer than SST_{wing}. This is mainly because the inappropriate warmer T_{sky} used for correcting the wing data, particularly under clear skies. Fig. 12 supports the arguments in Section III-C
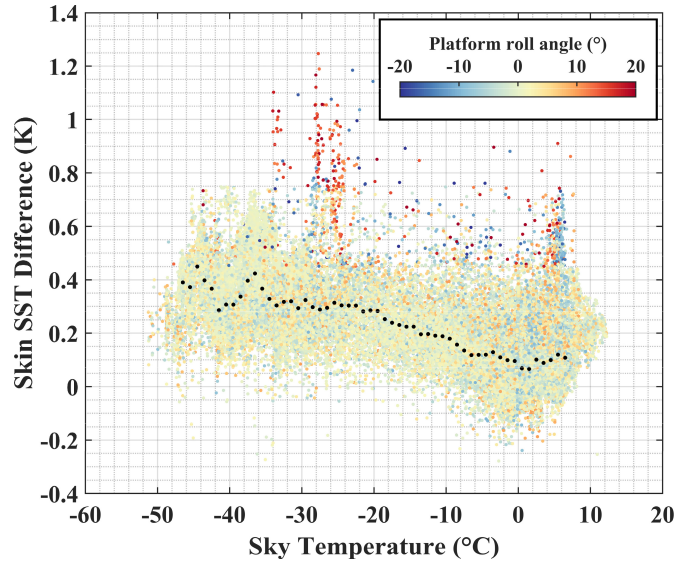

Fig. 12. SST_{hull} minus SST_{wing} as a function of sky temperature for the aggregate data of SD-1036 and SD-1037 without those close to the sea ice, colored by the platform roll angles. The black dots are the mean temperature differences in the small bins (1 °C) of sky temperatures.

that the SST_{skin} errors due to θ_e difference between up- and down-looking IR pyrometers under overcast skies are comparable to those under clear skies. Note that it also shows a dependence on sky temperature. This is largely due to clusters of temperature differences below zero under cloudy skies, which may indicate rain on the lens of the sky-viewing sensor. When rain droplets are on the surface of the lens, the measured T_{sky} tends to have a warm bias due to the higher temperature of raindrops. Given the larger correction for the reflected component in the derivation of SST_{hull}, a higher estimate of T_{sky} caused by rain on the lens of the up-looking radiometer results in $SST_{hull} < SST_{wing}$.

Unlike some shipborne radiometers, those on Saildrones did not have protective mechanisms to keep the up-looking optics clean and dry. However, there were modifications to the design of the CT09s aboard, including a shortened lens barrel with a chamfer to allow water to run off the lens surface (B. Foran, Wintronics Inc., pers. comm., 2021). In addition, the cameras give clear indications, so measurements made during and after rain could be screened out. As shown in Fig. 12, many large differences between SST_{hull} and SST_{wing} are characterized by large roll angles of the vehicle. The heeling effects have been partly eliminated by the constraints of θ_e in Section III-C, yet, some cases remain. Without considering pitching, θ_e of CT09 increases from 50° with roll angles, leading to T_{sky} with a more significant warm bias for the SST_{wing} derivation, especially under clear skies. The analyses above assume homogenous horizontal atmospheric conditions that radiative transfer at the spectral interval predominantly varies with zenith angles; however, it is not always the case in reality. Thus, SST_{wing} is possibly overcompensated with a colder T_{sky} than expected. The location of the wing CT15 seems to be advantageous in view of the smaller θ_e with less ε sensitivity to the θ_e variation due to Saildrone tilting, which can sufficiently reduce the

TABLE II
EFFECTIVE WAVELENGTHS FOR BAND-AVERAGED SEA SURFACE EMISSIVITY, SEA SURFACE EMISSION, AND DOWNWELLING SKY RADIANCE

	Emissivity	Sea Emission	Sky Radiance
Effective	11.90 ~ 12.02	8.65 ~ 9.07	8.55 ~ 10.25
Wavelength		or	or
Range (μm)		12.27 ~ 12.78	12.24 ~ 16.80

inaccuracy of T_{sky} and the resulting SST_{skin} error. Nonetheless, a direct reflection of the vehicle superstructure at the sea surface and into the FOV of the sea-viewing pyrometer is more significant at small θ_e [48]. Moreover, small θ_e means that it becomes more difficult to view a sea surface free of the vessels' bow wave.

B. Effect of the Broad Bandwidth of the Heitronics Pyrometers

For those shipborne radiometers using a narrow spectral waveband to derive SST_{skin}, $B(T, \lambda)$ and $\varepsilon(\lambda, \theta)$ are much less dependent on the wavelength change across the bandwidth. Therefore, (7) can be taken to a good approximation as

$$R_{sea} = \bar{\sigma} \left[\varepsilon(\bar{\lambda}, \theta) B(T_s, \bar{\lambda}) + (1 - \varepsilon(\bar{\lambda}, \theta)) B(T_{sky}, \bar{\lambda}) \right] \quad (11)$$

where $\bar{\sigma}$, $\varepsilon(\bar{\lambda}, \theta)$, $B(T_s, \bar{\lambda})$, and $B(T_{sky}, \bar{\lambda})$ are the band-averaged RSR, sea surface emissivity, sea surface emission, and downwelling atmospheric radiance at the surface, given by

$$\bar{\sigma} = \int_{\lambda_0}^{\lambda_1} \sigma(\lambda) d\lambda \quad (12)$$

$$\bar{\sigma} f(\bar{\lambda}) = \int_{\lambda_0}^{\lambda_1} \sigma(\lambda) f(\lambda) d\lambda \quad (13)$$

where $f(\lambda)$ could represent $\varepsilon(\lambda, \theta)$, $B(T_s, \lambda)$ or $B(T_{sky}, \lambda)$.

To test the effectiveness of this approximation on Saildrone radiometric measurements, we use (11) to determine the SST_{skin}. The SST_{hull} derived from the simplified equation generally deviates from that derived from (7) by >0.1 K. Such a visible difference is caused by the wide bandwidths of the Heitronics IR pyrometers used. Specifically, (11) only holds when $\bar{\lambda}$, the effective band-averaged wavelengths, for $\varepsilon(\bar{\lambda}, \theta)$, $B(T_s, \bar{\lambda})$, and $B(T_{sky}, \bar{\lambda})$ are identical or very nearly the same. However, due to the broad waveband causing large variabilities of emissivity and Planck function, the $\bar{\lambda}$ values for those three terms are inconsistent shown in Table II. The small ranges of $\bar{\lambda}$ for ε and surface emission are because of the relatively less variable zenith angles (after the constraints of θ_e) and skin temperatures, whereas $\bar{\lambda}$ for the sky radiance changes greatly due to varying atmospheric conditions. It is not surprising that there are always two $\bar{\lambda}$ solutions for the band-averaged Planck function at a certain temperature. This further demonstrates the use of (11) for the Saildrone SST_{skin} derivation is inappropriate. In conclusion, to access the Saildrone SST_{skin} with better accuracy, a more computational cost but rigorous way as (7) has to be chosen.

C. Uncertainty Budget Analysis

According to (7), the errors of Saildrone-derived SST_{skin} (here we refer specifically to SST_{hull}) have three main components: inaccuracies in sea surface emissivity determination and the uncertainties in both sea- and sky-viewing radiometric measurements. For $\varepsilon(\lambda, \theta)$, θ must be considered as θ_e due to the rolling and pitching of the vehicles, especially for IR pyrometers on the hull since ε decreases more rapidly for zenith angles >40°. As a result, ε values in the spectral interval of concern are simulated using the IREMIS model built into RTTOV for each data sample, given the knowledge of viewing geometry. The uncertainty could result from the tilted facets of the sea surface reflecting the downwelling atmospheric radiance deviating from θ_e; however, we assume that the relationship between wind speed and the tilts of facets caused by wind-generated waves implicit in the IREMIS model is appropriate for our conditions. Therefore, we assume that the uncertainty in the emissivity calculation is very small compared to other sources of inaccuracy. Besides the instrumental uncertainty of CT09, the measured T_{sky} introduces errors in SST_{skin} since its RSR function differs from that of CT15, and it has a different viewing angle from that of the paired down-looking CT15 when the platform is pitching, while the RSR function difference likely causes some small biases rather than uncertainty in SST_{skin}, as analyzed in Section III-C. The CT15 measurements contribute to the SST_{skin} uncertainty budget only due to the instrumental uncertainty. Since those contributions mentioned above are all random and independent of each other, the uncertainty budget for the Saildrone-derived SST_{skin} is given by

$$\epsilon_{skin}^2 = \epsilon_{sea}^2 + \epsilon_{sky}^2 + \epsilon_{angle}^2. \quad (14)$$

For the shipborne radiometers, the last term on the right-hand side of (14) is usually insignificant or zero. For Saildrones, the magnitude of the last term is effectively controlled by rejecting data under large platform tilt angles. As shown in Table I, the measurement uncertainty given in the manufacturer's specifications for the CT15 IR pyrometer is ±0.5 K plus 0.7% of the difference between target and instrument temperatures. Considering the temperature difference dependence of the measurement inaccuracies, the air temperature is generally within ±2 K of the SST_{skin}. The radiometer temperature is warmer than the air temperature, by typically 8 K–10 K (B. Foran, Wintronics Inc., pers. comm., 2022). Given that the Saildrone CT15 is likely to effectively lose heat to the air, we take the internal temperature to be 8 K above ambient, and when added to 2 K air–sea temperature difference, it gives a 10 K instrument-to-target temperature difference and a measurement error of 0.07 K. For the CT09 sky measurement, the target to instrument temperature difference could be as large as −50 K (see Fig. 12), leading to an extra measurement error of −0.3 K. Combining the last two terms in (14), T_{sky} introduces inaccuracies in the SST_{skin} retrievals ≤ 0.024 K for both SD-1036 and SD-1037 under clear skies. The accuracy requirement of the sea-viewing CT15 measurements must be much more stringent since the uncertainties propagate directly into the derivation of SST_{skin},
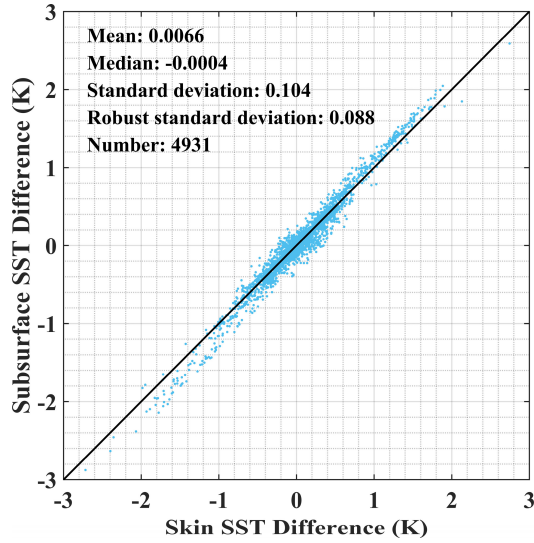
Fig. 13. SST_{skin} differences between SD-1036 and SD-1037 are plotted with the $SST_{0.3\,m}$ differences simultaneously measured by the SBE 56 temperature loggers mounted on the keel at a depth of 0.3 m when the separations of two Saildrones were within 10 km during the mission. The diurnal warming signals for both vehicles have been removed. The statistics on the upper left show the comparisons of those two sets of SST differences.

and the manufacturer's specifications are not an acceptable accuracy for the Saildrone SST_{skin} to validate the satellite-retrieved SST_{skin} values. Although the specifications of the manufacturer are generally believed to be very conservative, the actual values are undetermined because the pyrometers lacked laboratory calibrations before and after deployment, relying on the manufacturer's calibration certificate. However, there is an alternative way to make the first-order approximation of the instrumental accuracy based on the field data. Considering that SD-1036 and SD-1037 were close, within 10 km, at times during the 2019 Arctic Cruise, analyzing contemporaneous subsurface SSTs from both vehicles provides information on the geophysical variability of SST over these short spatial scales. The subsurface SSTs from Sea-Bird SBE 56 temperature loggers installed on the keels of the Saildrones at a depth of 0.324 m were measured to high accuracy, 0.002 K, and thus, larger differences between the SST measurements from two Saildrones can be attributed to spatial variability. The uncertainty of SST_{skin} can be evaluated by comparing ΔSST_{skin}, including an uncertainty term u_c and the $\delta(SST_{skin})$ term due to geophysical variability in (15), with the corresponding $\Delta SST_{0.3\,m}$, which only contains the geophysical variability $\delta(SST_{0.3\,m})$ in (16), from two Saildrones and making the assumption of a consistent uppermost ocean thermal structure given in (17). For this hypothesis to hold, periods with signals indicative of diurnal warming (SST_{skin} warmer than $SST_{0.3\,m}$) in the measurements from either SD-1036 or SD-1037, or both, have been removed to minimize the contribution of thermal stratification variations to the comparisons. In Fig. 13, ΔSST_{skin} shows a good agreement with the $\Delta SST_{0.3\,m}$, and the large temperature divergences indicate the probable effects of oceanic fronts between the two Saildrones. The uncertainty of SST_{skin} is thus estimated to be

about 0.122 K at a confidence level of 95% (multiplied by a weight factor of 1.96) using the statistics of robust standard deviation, as shown in (18), which is a more robust metric calculated as the interquartile range divided by 1.35, and assuming that the SST_{skin} uncertainties for SD-1036 (u_{1036}) and SD-1037 (u_{1037}) are identical given in (19)

$$\Delta SST_{skin} = SST_{skin\_1036} - SST_{skin\_1037} = u_c + \delta(SST_{skin})$$
(15)

$$\Delta SST_{0.3\,m} = SST_{0.3\,m\_1036} - SST_{0.3\,m\_1037} = \delta(SST_{0.3\,m}) \quad (16)$$

$$\delta(SST_{skin}) = \delta(SST_{0.3\,m}) \quad (17)$$

$$u_c = \sqrt{u_{1036}^2 + u_{1037}^2} = 1.96$$
$$\quad * RSD(\Delta SST_{skin} - \Delta SST_{0.3\,m}) \quad (18)$$

$$u_{SST_{skin}} = u_{1036} = u_{1037}. \quad (19)$$

The assessment above demonstrates that the accuracy of the CT15 instrument on Saildrones is $\sim$0.12 K, much better than the 0.5 K (plus 0.07 K) given in the manufacturer's specification. Nevertheless, this CT15 instrumental uncertainty is the largest component of the errors in the SST_{skin} retrievals. There could be some systematic biases in the radiometer measurements that would not necessarily be revealed in this analysis, and this concern led us to conduct a laboratory calibration of the same type of sea-viewing radiometer. If this configuration of radiometric temperature measurements is to be used in future Saildrone missions, then rigorous laboratory calibration before and after deployment should be a priority.

D. Calibration of Heitronics CT15 Pyrometer

Given that the uncertainty of the Heitronics CT15 pyrometer has been revealed likely to be much smaller than the manufacturer's specification (see Table I), we decided to calibrate the instrument against SI-traceable IR laboratory calibration facilities at the University of Miami's Rosenstiel School of Marine, Atmospheric, and Earth Science [49], [50] to further assess the absolute accuracy and noise levels of the measurements. The sensors installed on the SD-1036 or SD-1037 were not available, but Saildrone Inc. provided one of the same type, SN12718, for our lab calibration. The calibration was conducted using a stabilized water-bath blackbody target built to a National Institute of Standards and Technology (NIST) design comprising a tapered, thin copper cone with a 10.8-cm diameter aperture [51]. The temperature of the blackbody was monitored by two reference thermometers connected to a Black Stack interface unit, which underwent a system calibration at Fluke[1] Calibration resulting in measuring errors <5 mK, and an uncertainty <2 mK. The temperature drop across the copper cone with a high emissivity ($\sim$0.999) paint is <1 mK and has a dependence on the water to ambient temperature difference [51].

The measurements were taken at eight set points from 15 °C to 50 °C at 5 °C intervals, and they were analyzed for periods when the water-bath blackbody temperature had stabilized; the sample size of the blackbody at each set point ranged from 701 to 1753 (5-s sampling) and from 2451 to
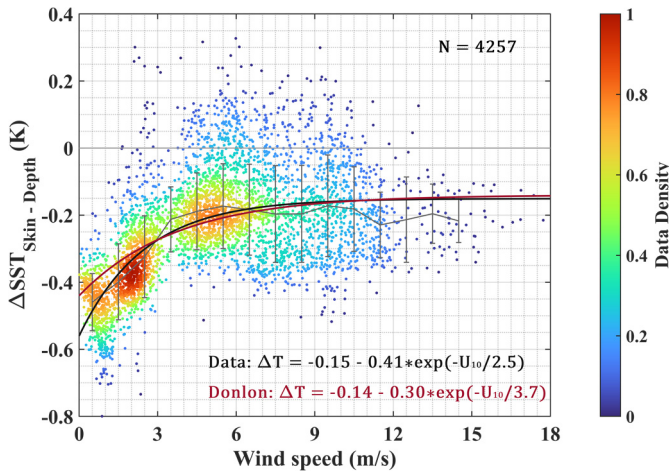
---

[1]Registered trademark.

Fig. 14. Nighttime SD-1036 and SD-1037 SST_{skin} minus $SST_{-1.71\,m}$ as a function of 10-m wind speed. The least-squares fit curve is shown in black, and the formula from [52] is plotted in red. The mean and standard deviation of temperature differences, calculated at 1-m/s intervals, are shown as gray lines and error bars, respectively.

6051 for the CT15 (3-s sampling). The standard deviations of the water-bath temperatures were <0.5 mK and the CT15 measurements <0.02 K, which could support the estimations in Section IV-C. As expected, the CT15 data were cooler than those for the water bath. There was an approximatively linear relationship between the errors of CT15 data and the blackbody to ambient temperature differences, confirming the manufacturer's statement of a dependence of the measurement errors increasing with the temperature difference between the target and the instrument. The Rosenstiel School calibration did reveal a negative error of ∼0.13 K at blackbody temperatures close to ambient in the laboratory. While this is well within the accuracy specification of the manufacturer, it is large in comparison with the target accuracy (<0.1 K) for scientific applications of SST_{skin}. One of the limitations of the Rosenstiel School calibration is the inability to cool the blackbody temperature much below ambient before condensation occurs on the surface of the cone of the blackbody.

Wintronics Inc., the U.S. agent for Heitronics, has calibration facilities that can reach cold temperatures, and they offered to calibrate the CT15 used in our calibration. The result at their blackbody target temperature of 1 °C was +0.09 K and −0.07 K at 30 °C (B. Foran, Wintronics Inc., pers. comm., 2022). Assuming a monotonic temperature dependence of the error, the measurement errors at temperatures experienced in the 2019 Saildrone deployments were ∼0.06 K on average. The same CT15 was calibrated at Heitronics in 2018 prior to delivery to Saildrone Inc., and the error at 1 °C was 0.11 K, indicating that the calibration drift over time of this CT15 was negligible. The cold temperature calibration at Wintronics is reassuring, but, of course, these calibrations were not of instruments used in the 2019 deployment. To summarize, the measuring errors of the CT15s used for the sea-viewing observations on the Saildrones in the 2019 deployments are very likely to be <0.1 K.

Furthermore, a convincing demonstration of the absolute accuracy of the 2019 Arctic Saildrone SST_{skin} values resulted from an analysis of SST_{skin} compared to $SST_{1.7\,m}$, the deepest temperature taken by SBE 56 logger, in conditions without evidence of diurnal heating, as a function of 10-m wind speed, revealing a distribution that is congruent with other published results [52], [53] (see Fig. 14). The curve fit to the Saildrone data has an asymptotic value at high winds that differ from [52] by 0.01 K and from [53] by 0.02 K. Therefore, it would be very unlikely if there were a significant systematic error in the Saildrone-derived SST_{skin}.

V. CONCLUSION

The 2019 Saildrone Arctic Cruise was for 150 days from Dutch Harbor, Alaska, passing through the Bering Strait and the Chukchi Sea to the southern sea ice edge of the Arctic Ocean and back from May 15 to October 11. The fleet comprised six Saildrones, four of which were deployed by NOAA PMEL [39], [54]. Two MISST Saildrones (SD-1036 and SD-1037) were equipped with "unicorn"-style IR radiation pyrometers manufactured by Heitronics mounted on the deck. Using both the sea- and sky-viewing measurements and the sea surface emissivity (ε) values simulated by the IREMIS model built into the RTTOV, the Saildrone SST_{skin} can be derived from (7). To obtain sufficiently accurate ε, the viewing geometry of sensors must be well established given the effects of vehicles' pitching and rolling on the measurements. The SST_{skin} retrievals are highly likely to be contaminated when the Saildrones were close to, or trapped in sea ice, and also during, and for some time after rainfall. Both the cases of approaching sea ice and precipitation events were recorded by the four cameras on the Saildrones permitting the data to be removed. Analyzing the contributions to the inaccuracy of SST_{skin} indicates the errors mainly come from both CT09 and CT15 radiometric temperatures, as described in Section IV-C, and the largest component is instrumental uncertainty of the CT15 data. Our analyses indicate that the accuracy of CT15 measurements is much better than 0.5 K provided in the manufacturer's specifications, and this is also supported by the laboratory calibration for a CT15 SN12718 at the Rosenstiel School and especially at low temperatures at Wintronics Inc. For the sky temperatures from the CT09 radiometers, besides instrumental uncertainty, the different RSR functions and inconsistent viewing angles due to the pitching of the Saildrones between CT09 and CT15 also introduce errors in SST_{skin}, which are typically absent in shipborne radiometer systems, such as the M-AERI and ISAR. Generally, the CT09 introduced SST_{skin} errors are minor by virtue of the small reflectivity of the ocean surface. Nevertheless, based on LBLRTM radiative transfer simulations, the up- and down-viewing angle differences must be constrained within a few degrees. In addition, the error resulting from RSR function discrepancy can be negligible for SD-1036 but should be accounted for SD-1037. The SST_{skin} derived from the hull IR pyrometers has an estimated uncertainty of 0.12 K, with insignificant mean bias, which is sufficiently accurate to study many aspects of the upper-ocean thermal skin layer, air–sea heat exchanges, and oceanic thermal front patterns and to validate satellite-retrieved SST_{skin}, especially at high

latitudes as shown here, and probably elsewhere. Despite the lack of comparisons with data from well-accepted shipborne IR radiometer systems within small spatiotemporal windows, the Saildrone SST_{skin} derived from data collected during the Arctic Cruise in 2019 has been exhibited to make stable measurements with useful accuracy. In view of the lower costs and good capabilities, Saildrones display potential advantages for collecting SST_{skin} data.

APPENDIX

The Saildrone-derived SST_{skin} data are openly available from the University of Miami Libraries at https://doi.org/10.17604/jnvv-nm74.

The data for the 2019 Saildrone Arctic Cruise are openly available from the NASA PO.DAAC at https://doi.org/10.5067/SDRON-NOPP0.

The reanalysis MERRA-2 data used in this study are openly available from the Goddard Earth Sciences Data and Information Services Center at https://doi.org/10.5067/3Z173KIE2TPD and https://doi.org/10.5067/WWQSXQ8IVFW8.

ACKNOWLEDGMENT

REFERENCES

[1] P. Tandeo, B. Chapron, S. Ba, E. Autret, and R. Fablet, "Segmentation of mesoscale ocean surface dynamics using satellite SST and SSH observations," *IEEE Trans. Geosci. Remote Sens.*, vol. 52, no. 7, pp. 4227–4235, Jul. 2014.

[2] M. W. Buckley, R. M. Ponte, G. Forget, and P. Heimbach, "Low-frequency SST and upper-ocean heat content variability in the North Atlantic," *J. Climate*, vol. 27, no. 13, pp. 4996–5018, Jul. 2014.

[3] R. Parfitt, A. Czaja, and Y.-O. Kwon, "The impact of SST resolution change in the ERA-interim reanalysis on wintertime Gulf stream frontal air-sea interaction," *Geophys. Res. Lett.*, vol. 44, no. 7, pp. 3246–3254, Apr. 2017.

[4] H. R. Pethybridge et al., "Spatial patterns and temperature predictions of tuna fatty acids: Tracing essential nutrients and changes in primary producers," *PLoS ONE*, vol. 10, no. 7, Jul. 2015, Art. no. e0131598.

[5] S. Schlunegger et al., "Emergence of anthropogenic signals in the ocean carbon cycle," *Nature Climate Change*, vol. 9, no. 9, pp. 719–725, Sep. 2019.

[6] A. P. Cracknell, "The advanced very high resolution radiometer (AVHRR)," *Oceanographic Literature Rev.*, vol. 44, no. 5, p. 526, 1997.

[7] D. Llewellyn-Jones, M. C. Edwards, C. T. Mutlow, A. R. Birks, I. J. Barton, and H. Tait, "AATSR: Global-change and surface-temperature measurements from Envisat," *ESA Bull.-Eur. Space Agency*, vol. 105, p. 11, Feb. 2001.

[8] P. J. Minnett, R. H. Evans, E. J. Kearns, and O. B. Brown, "Sea-surface temperature measured by the moderate resolution imaging spectroradiometer (MODIS)," in *Proc. IEEE Int. Geosci. Remote Sens. Symp.*, vol. 2, Jun. 2002, pp. 1177–1179.

[9] P. Coppo et al., "SLSTR: A high accuracy dual scan temperature radiometer for sea and land surface monitoring from space," *J. Modern Opt.*, vol. 57, no. 18, pp. 1815–1830, Oct. 2010.

[10] B. Luo, P. J. Minnett, M. Szczodrak, K. Kilpatrick, and M. Izaguirre, "Validation of Sentinel-3A SLSTR derived sea-surface skin temperatures with those of the shipborne M-AERI," *Remote Sens. Environ.*, vol. 244, Jul. 2020, Art. no. 111826.

[11] P. J. Minnett et al., "Skin sea-surface temperature from VIIRS on Suomi-NPP—NASA continuity retrievals," *Remote Sens.*, vol. 12, no. 20, p. 3369, Oct. 2020.

[12] C. Donlon et al., "Successes and challenges for the modern sea surface temperature observing system," in *Proc. OceanObs, Sustained Ocean Observ. Inf. Soc.*, vol. 2, 2010, pp. 1–9.

[13] J. A. Curry, J. L. Schramm, W. B. Rossow, and D. Randall, "Overview of Arctic cloud and radiation characteristics," *J. Climate*, vol. 9, no. 8, pp. 1731–1764, Aug. 1996.

[14] C. Jia and P. J. Minnett, "High latitude sea surface temperatures derived from MODIS infrared measurements," *Remote Sens. Environ.*, vol. 251, Dec. 2020, Art. no. 112094.

[15] L. R. Centurioni et al., "Global in situ observations of essential climate and ocean variables at the air–sea interface," *Frontiers Mar. Sci.*, vol. 6, p. 419, Aug. 2019, doi: 10.3389/fmars.2019.00419.

[16] C. J. Donlon, M. Martin, J. Stark, J. Roberts-Jones, E. Fiedler, and W. Wimmer, "The operational sea surface temperature and sea ice analysis (OSTIA) system," *Remote Sens. Environ.*, vol. 116, pp. 140–158, Jan. 2012.

[17] M. C. Serreze and R. G. Barry, "Processes and impacts of Arctic amplification: A research synthesis," *Global Planet. Change*, vol. 77, nos. 1–2, pp. 85–96, May 2011.

[18] M. Rantanen et al., "The Arctic has warmed nearly four times faster than the globe since 1979," *Commun. Earth Environ.*, vol. 3, no. 1, p. 168, Aug. 2022.

[19] R. F. Vincent, "The case for a single channel composite Arctic sea surface temperature algorithm," *Remote Sens.*, vol. 11, no. 20, p. 2393, Oct. 2019.

[20] J. L. Høyer, I. Karagali, G. Dybkjær, and R. Tonboe, "Multi sensor validation and error characteristics of Arctic satellite sea surface temperature observations," *Remote Sens. Environ.*, vol. 121, pp. 335–346, Jun. 2012.

[21] S. L. Castro, G. A. Wick, and M. Steele, "Validation of satellite sea surface temperature analyses in the Beaufort Sea using UpTempO buoys," *Remote Sens. Environ.*, vol. 187, pp. 458–475, Dec. 2016.

[22] F. Xu and A. Ignatov, "In situ SST quality monitor (iQuam)," *J. Atmos. Ocean. Technol.*, vol. 31, no. 1, pp. 164–180, Jan. 2014.

[23] P. M. Saunders, "The temperature at the ocean-air interface," *J. Atmos. Sci.*, vol. 24, no. 3, pp. 269–273, May 1967.

[24] P. Flament, J. Firing, M. Sawyer, and C. Trefois, "Amplitude and horizontal structure of a large diurnal sea surface warming event during the coastal ocean dynamics experiment," *J. Phys. Oceanogr.*, vol. 24, no. 1, pp. 124–139, 1994.

[25] C. L. Gentemann, P. J. Minnett, P. Le Borgne, and C. J. Merchant, "Multi-satellite measurements of large diurnal warming events," *Geophys. Res. Lett.*, vol. 35, no. 22, pp. 1–6, 2008.

[26] S. Eastwood, P. Le Borgne, S. Péré, and D. Poulter, "Diurnal variability in sea surface temperature in the Arctic," *Remote Sens. Environ.*, vol. 115, no. 10, pp. 2594–2602, Oct. 2011.

[27] P. J. Minnett, "Radiometric measurements of the sea-surface skin temperature: The competing roles of the diurnal thermocline and the cool skin," *Int. J. Remote Sens.*, vol. 24, no. 24, pp. 5033–5047, 2003.

[28] J. W. Bennett, "CSIRO single channel infrared radiometer model DAR011," in *CSIRO Division of Atmospheric Research Internal Paper*, vol. 3195. Aspendale, VIC, Australia: CSIRO Division of Atmospheric Research, 1998.

[29] C. J. Donlon, T. Nightingale, L. Fiedler, G. Fisher, D. Baldwin, and I. S. Robinson, "The calibration and intercalibration of sea-going infrared radiometer systems using a low cost blackbody cavity," *J. Atmos. Ocean. Technol.*, vol. 16, no. 9, pp. 1183–1197, Sep. 1999.

[30] C. J. Donlon et al., "Solid-state radiometer measurements of sea surface skin temperature," *J. Atmos. Ocean. Technol.*, vol. 15, no. 3, pp. 775–787, Jun. 1998.

[31] P. J. Minnett, R. O. Knuteson, F. A. Best, B. J. Osborne, J. A. Hanafin, and O. B. Brown, "The marine-atmospheric emitted radiance interferometer: A high-accuracy, seagoing infrared spectroradiometer," *J. Atmos. Ocean. Technol.*, vol. 18, pp. 994–1013, Jun. 2001.

[32] A. T. Jessup and R. Branch, "Integrated ocean skin and bulk temperature measurements using the calibrated infrared in situ measurement system (CIRIMS) and through-hull ports," *J. Atmos. Ocean. Technol.*, vol. 25, no. 4, pp. 579–597, Apr. 2008.

[33] C. J. Donlon et al., "An infrared sea surface temperature autonomous radiometer (ISAR) for deployment aboard volunteer observing ships (VOS)," *J. Atmos. Ocean. Technol.*, vol. 25, no. 1, pp. 93–113, Jan. 2008.

[34] C. L. Gentemann et al., "MISST: The multi-sensor improved sea surface temperature project," *Oceanography*, vol. 22, no. 2, pp. 76–87, 2009.

[35] C. L. Gentemann et al., "Arctic MISST: Multi-sensor improved sea surface temperature: Continuing the GHRSST partnership and improving Arctic data," *Presented at the AGU Fall Meeting*, vol. 1, Washington, DC, USA, 2018. [Online]. Available: https://ui.adsabs.harvard.edu/abs/2018AGUFM.A24K.11G

[36] J. Thomson, J. B. Girton, R. Jha, and A. Trapani, "Measurements of directional wave spectra and wind stress from a wave glider autonomous surface vehicle," *J. Atmos. Ocean. Technol.*, vol. 35, no. 2, pp. 347–363, Feb. 2018.

[37] J. Manley and S. Willcox, "The wave glider: A persistent platform for ocean science," in *Proc. IEEE OCEANS*, Sydney, NSW, Australia, May 2010, pp. 1–5.

[38] C. L. Gentemann et al., "Saildrone: Adaptively sampling the marine environment," *Bull. Amer. Meteorolog. Soc.*, vol. 101, no. 8, pp. 744–762, Aug. 2020.

[39] C. Meinig et al., "Public–private partnerships to advance regional ocean-observing capabilities: A saildrone and NOAA-PMEL case study and future considerations to expand to global scale observing," *Frontiers Mar. Sci.*, vol. 6, p. 448, Aug. 2019.

[40] T. M. Chin, J. Vazquez-Cuervo, and E. M. Armstrong, "A multi-scale high-resolution analysis of global sea surface temperature," *Remote Sens. Environ.*, vol. 200, pp. 154–169, Oct. 2017.

[41] R. Saunders et al., "An update on the RTTOV fast radiative transfer model (currently at version 12)," *Geosci. Model Develop.*, vol. 11, no. 7, pp. 2717–2737, 2018.

[42] S. M. Newman, J. A. Smith, M. D. Glew, S. M. Rogers, and J. P. Taylor, "Temperature and salinity dependence of sea surface emissivity in the thermal infrared," *Quart. J. Roy. Meteorolog. Soc.*, vol. 131, no. 610, pp. 2539–2557, Jul. 2005.

[43] R. Saunders et al. (2017). *RTTOV v12 Science and Validation Report*. [Online]. Available: https://www.nwpsaf.eu/site/download/documentation/rtm/docs_rttov12/rttov12_svr.pdf

[44] L. Palchetti et al., "FORUM: Unique far-infrared satellite observations to better understand how earth radiates energy to space," *Bull. Amer. Meteorolog. Soc.*, vol. 101, no. 12, pp. 2030–2046, Dec. 2020.

[45] S. A. Clough et al., "Atmospheric radiative transfer modeling: A summary of the AER codes," *J. Quant. Spectrosc. Radiat. Transf.*, vol. 91, no. 2, pp. 233–244, 2005.

[46] R. Gelaro et al., "The modern-era retrospective analysis for research and applications, version 2 (MERRA-2)," *J. Climate*, vol. 30, pp. 5419–5454, Jul. 2017.

[47] F. Chevallier, S. D. Michele, and A. McNally, "Diverse profile datasets from the ECMWF 91-level short-range forecasts," Eur. Centre Medium-Range Weather Forecasts, Shinfield Park, Reading, Tech. Rep. NWPSAF-EC-TR-010, 2006. [Online]. Available: https://www.ecmwf.int/node/8685.

[48] C. J. Donlon et al., "Ship-borne thermal infrared radiometer systems," in *Experimental Methods in the Physical Sciences*, vol. 47, G. Zibordi, C. J. Donlon, and A. C. Parr, Eds. New York, NY, USA: Academic, 2014, pp. 305–404.

[49] J. P. Rice et al., "The Miami2001 infrared radiometer calibration and intercomparison. Part I: Laboratory characterization of blackbody targets," *J. Atmos. Ocean. Technol.*, vol. 21, no. 2, pp. 258–267, Feb. 2004.

[50] E. Theocharous, I. Barker-Snook, and N. P. Fox, "2016 comparison of IR brightness temperature measurements in support of satellite validation. Part 1: Blackbody Laboratory comparison," Nat. Phys. Lab., Teddington, Middlesex, U.K., 2017, [Online]. Available: http://www.frm4sts.org/wp-content/uploads/sites/3/2017/12/FRM4STS_D100_TR-2_Part1_Blackbody_23Jun17-signed.pdf

[51] J. B. Fowler, "A third generation water bath based blackbody source," *J. Res. Nat. Inst. Standards Technol.*, vol. 100, no. 5, pp. 591–599, 1995.

[52] C. J. Donlon et al., "Toward improved validation of satellite sea surface skin temperature measurements for climate research," *J. Climate*, vol. 15, no. 4, pp. 353–369, Feb. 2002.

[53] P. J. Minnett, M. Smith, and B. Ward, "Measurements of the oceanic thermal skin effect," *Deep Sea Res. II, Topical Stud. Oceanogr.*, vol. 58, no. 6, pp. 861–868, 2011.

[54] A. M. Chiodi et al., "Exploring the Pacific Arctic seasonal ice zone with saildrone USVs," *Frontiers Mar. Sci.*, vol. 8, pp. 1–20, Mar. 2021.

Chong Jia received the B.S. degree in oceanic and atmospheric sciences from the Ocean University of China, Qingdao, China, in 2017, and the M.Sc. degree in meteorology and physical oceanography from the University of Miami, Miami, FL, USA, in 2019, where he is currently pursuing the Ph.D. degree in meteorology and physical oceanography.

His research interests include ship-board remote sensing instrumentation, satellite sea surface temperature remote sensing, physics of the upper ocean, and air–sea interactions.

Peter J. Minnett received the B.A. degree in physics from the University of Oxford, Oxford, U.K., in 1973, and the M.Sc. and Ph.D. degrees in oceanography from the University of Southampton, Southampton, U.K., in 1975 and 1978, respectively.

In 1995, he joined the University of Miami, Miami, FL, USA, becoming a Professor Emeritus of ocean sciences at the Rosenstiel School of Marine, Atmospheric, and Earth Science in 2021. His research interests include deriving accurate measurements of ocean variables, primarily sea surface temperature, by remote sensing from satellites and ships.

Dr. Minnett has served as the Science Team Chair of the Group for High Resolution Sea-Surface Temperature from 2012 to 2016.

Malgorzata Szczodrak received the M.Sc. degree in physics from Jagiellonian University, Kraków, Poland, in 1987, and the Ph.D. degree from the Atmospheric Science Programme, The University of British Columbia, Vancouver, BC, Canada, in 1998.

She is currently an Associate Scientist with the Department of Ocean Sciences, Rosenstiel School of Marine, Atmospheric, and Earth Science, University of Miami, Miami, FL, USA. Her research focuses on ship-based infrared (IR) measurements of sea surface temperature and algorithm development, as well as the validation of satellite sea surface temperature (SST) products for the Moderate Resolution Imaging Spectroradiometer (MODIS) and the Visible Infrared Imaging Radiometer Suite (VIIRS).

Miguel Izaguirre received the B.S. degree in biology from Metropolitan Autonomous University, Mexico City, Mexico, in 1980, and the MALS degree from the University of Miami, Miami, FL, USA, in 2014.

He is currently a Research Associate with the Department of Ocean Sciences, Rosenstiel School of Marine, Atmospheric, and Earth Science, University of Miami. His research interests include climatology, data science and computing, and machine learning and automation.